Final Draft Post Referee - Surf. Coat Techn., **324** 36-47 (2017)

Lifetime and Failure Modes of Plasma Sprayed Thermal Barrier Coatings in Thermal Gradient Rig Tests with Simultaneous CMAS Injection

Daniel E. Mack[1*], Tanja Wobst[1,2], Maria Ophelia D. Jarligo[1,3], Doris Sebold[1], Robert Vaßen[1]

[1]Forschungszentrum Jülich GmbH, Institute Of Energy and Climate Research, Materials Synthesis and Processing (IEK-1), 52425 Jülich, Germany

Abstract

Degradation of thermal barrier coatings (TBCs) in gas-turbine engines due to calcium–magnesium–aluminosilicate (CMAS) glassy deposits from various sources such as sand, volcanic ash, fly ash, or variable quality fuels has been a tenacious issue during the recent years. This follows from the fact that engines are required to operate under increasingly harsh conditions in all kind of gas turbine applications following the demands for higher efficiency and operational flexibility. While the understanding of the mechanism of CMAS induced degradation of TBCs as well as approaches for mitigation of CMAS attack by means of advanced TBC compositions have grown remarkably, most of the reported results have been obtained from lab testing at isothermal conditions or from evaluation of ex-service components, either. The isothermal tests are not reproducing important thermomechanical effects from service conditions, and it may be hard to figure out the thermal history of the ex-service examples.

In this study a burner rig facility has been used for the evaluation of TBC performance, where a thermal gradient is applied across the TBC at cyclic load and CMAS is continuously injected to the combustion environment to simulate the conditions closer to actual service in an engine while allowing control of important degradation limiting parameters. Tests have been performed on the state of the art material YSZ while loading parameters as high temperature dwell time and CMAS deposition rate have been varied. Tests have been evaluated in terms of chemical degradation, failure mode and TBC spallation lifetime by means of SEM, EDS and XRD. Test conditions and relevance to in-service operating conditions are discussed. Major impacts on thermal gradient cycling lifetime and similarities and discrepancies related to reported failure mechanism are reviewed.

Keywords

thermal barrier coatings (TBCs), atmospheric plasma spraying (APS), gradient burner rig test, calcium magnesium.alumino-silicate (CMAS), spallation lifetime

*corresponding author

Phone: +49 2461 61-2971

Fax: +49 2461 61-2455

E-Mail: d.e.mack@fz-juelich.de

Present adresses:

[2]Rolls Royce Deutschland Ltd & Co KG, Eschenweg 11, Dahlewitz, D-15827 Blankenfelde-Mahlow, Germany

[3]Quantiam Technologies Inc., 1651 - 94 Street NW, Edmonton, AB T6N 1E6, Canada

1 Introduction

Gas turbine efficiency has been increased over the last decades by major increases of turbine inlet temperatures and pressures. This has been driven by a successful development and application of advanced component cooling technologies as film cooling and thermal barrier coating (TBC) systems which can protect inside cooled metallic components from the extreme temperatures by establishing a thermal gradient across the coating’s thickness [1, 2]. For a functional temperature protection it is necessary that no blocking of cooling holes occurs and that the TBC system is intact and that it possesses a high effective thermal resistance. In that sense dust, sand, or general debris which entered into the turbine hot gas path for a long time only has been dangerous in respect to its ability to cause a mechanical blocking of functional holes and gaps and to cause erosion of the ceramic TBCs. With increasing turbine inlet temperatures a new mode of degradation of TBC started to be observed in the early 90s [3] which is caused by deposits from calcium-magnesium-aluminosilicates - so called CMAS. Those silicates are becoming molten in flight or on the TBC surfaces with temperatures well above 1200°C. In the liquid state they are able to intrude not only into cooling channels but also to easily infiltrate the intercolumnar gaps in electron beam physical vapor deposition (EB-PVD) TBCs or the open porosity of atmospheric plasma spray (APS) coatings. By that the amount of cooling flux is reduced, the net thermal conductivity of the ceramic TBC layer is increased, and the thermomechanical durability of the coating system is reduced [4].

The first occurrence of the CMAS phenomenon reported from gas turbines of helicopters operated in desert areas [5] can be attributed to the extreme concentration of the debris on the conditions of low altitude flights. Although hardly achievable for aero engines it seems likely that the problem can be handled by an improved filtering of the in-take air.

Meanwhile similar phenomena have also been observed caused by volcanic ash pollutants of much lower concentration as well as in the context of stationary gas turbines where intake air is filtered with limited efficiency. In the latter case the deposits originate from imperfect filtering, contaminants of low purity fuels, and wear debris from components all along the hot gas path [2].

The understanding of the mechanism of CMAS induced degradation of TBCs has grown remarkably from numerous studies over the recent years, summarized e.g. by Levi et al. [6]. Important conclusions are:

- If not large siliceous debris cause impact damage to TBCs, small debris can cause erosive wear or local spallation [7, 8].
- When the surface temperature of TBCs exceeds the CMAS melting point, a liquid phase is formed from the CMAS deposit [9-11]. If the debris is inhomogeneous or if the CMAS is not close to an eutectic composition, at the onset temperature of melting a mixture of an eutectic liquid plus remaining solid inclusions is formed until the temperature exceeds the liquidus temperature.
- The molten CMAS penetrates into TBCs due to remarkable wetting ability and low viscosity [10, 12, 13]. In some cases penetration even down to the substrate and attack of the thermally grown oxide (TGO), promoting detachment of TBCs, has been observed especially in the presence of sulphates [14-16].
- The porosity of the infiltrated ceramic layers is reduced, leading to an increase of the thermal conductivity [17] and on solidification and crystallization of the melt also to an increased stiffness [11, 18, 19].
- At elevated temperatures yttria-stabilized zirconia (YSZ) is partially dissolved by CMAS, resulting in microstructure degradation and phase transformation [20].

- CMAS attacks TBCs primarily via cold shock degradation mechanism [21, 22]. Upon cooling, CMAS solidifies, and the in-plane modulus of the CMAS-penetrated layer increases by a factor of 5–10. Such high modulus and low toughness of the TBC increase its susceptibility to cracking during thermal cycles [4, 23]. Cumulative cracks promoted by engine cycles lead to final spallation of TBCs [7].
- Failure of plasma sprayed TBCs through CMAS induced buckling has been observed in some cases [24, 25].

Although the consequences of those proposed degradation pathways in terms of changed response on thermomechanical loads during operation scenarios can be simulated in principle [26], a lifetime prediction accounting for CMAS degradation which would be beneficial e.g. for classification risk levels in air traffic is in an infantile state [8, 9]. This is to some extent due to the fact that important factors affecting the loading condition under operational conditions, as e.g. the deposition probability of ingested particles [27], are not yet comprehensively studied. Another source of uncertainty is the linking of the different degradation pathways leading to concurrent modes of catastrophic failure. Especially the latter invoked some demand for studying this interplay in appropriate controllable conditions as e.g. gradient rig testing [28-31].

Hence, the aim of this study is an improved understanding of the failure mechanism and spallation lifetime of TBCs under thermal conditions similar to the operation in a gas turbine environment, i.e. temperature gradient, cyclic thermomechanical loading, and continuous CMAS attack. This is expected to be beneficial for an assessment of remaining life of components being exposed to CMAS deposits as well as for the targeted development of TBCs with an improved durability under those operation conditions. A burner rig facility has been used, where a thermal gradient is applied across the TBC at cyclic load and CMAS is continuously injected to the combustion environment. Tests have been performed on the state of the art material YSZ while loading parameters as high temperature dwell time and CMAS deposition rate have been varied. Evaluation has been conducted in respect to chemical degradation, failure mode and TBC spallation lifetime by use of SEM, EDS and XRD. Validity of test conditions and relevance to operation conditions are discussed. Major focus has been given to the impacts of high temperature dwell times and the CMAS deposition rate which are expected to be closely correlated to the concurrent effects of corrosive and thermomechanical degradation, respectively.

2 Experimental

Specimens for use in thermal gradient burner rig tests were manufactured using discs from nickel based superalloy (30 mm in diameter and 3 mm in thickness). Prior to coating the substrates were machined to feature a rounded outer rim (radius 1.5 mm) aiming to reduce mechanical stresses at the edges, a central drilling for inserting a thermocouple, and a circumferential notch for fixing the sample during manufacture and test. The sandblasted substrates were coated with a MCrAlY (M=Ni,Co) bond coat of 150-230 µm thickness followed by a heat-treatment under vacuum conditions to increase bonding by inter-diffusion between substrate and the bond coat layer. In case of the specimens WDS2279-88, which were used in the series of cyclic lifetime testing to failure, 150µm of bondcoat from CoNiCrAlY feedstock of type Amdry995C (Oerlikon Metco, Switzerland) was applied by high velocity oxide fuel (HVOF) thermal spray process with a Diamant Jet spray gun using an industrial scale thermal spray facility (Multicoat, Oerlikon Metco, formerly Sulzer Metco, Wohlen, Switzerland). Heat treatment was done at temperatures of 1120°C and 845°C with dwell times of 2 hours and 24 hours, respectively, in accordance with the procedure adviced by the manufacturer for the used substrate material of IN738. In case of the specimens

WDS1753 and WDS2235 substrates of different sources were utilized with CoNiCrAlY bondcoat applied.

A ceramic top coat layer of 7YSZ was added by atmospheric plasma spraying (APS) with a Triplex Pro II plasma torch on the same Multicoat facility. Powder of type Metco 204NS (Oerlikon Metco, particle size range of -125 +11 µm) was used as feedstock for the ceramic top layer. Same coating parameter except the number of passes during deposition were used for all specimen to ensure comparable microstructure of the coatings. Top layer thickness of specimens WDS2279-88 was 440-460 µm. Those of specimens WDS1753 and WDS2235 was 320-340 µm. Free standing coatings were also deposited onto stainless steel and subsequently detached with hydrochloric acid. Porosity of free standing coatings was determined using mercury intrusion porosimetry (Pascal 140/440, Porotec, Germany). Specimens WDS2279-88 were processed in same or subsequent runs throughout the manufacturing to ensure a maximum of comparability in cyclic lifetime and failure modes to be discussed.

The degradation and performance of the coatings under CMAS attack was tested in a burner rig test under thermal gradient conditions with a continuous deposition of CMAS onto the heated ceramic surface. Constituents of CMAS deposits were injected into the flame by means of a water-based precursor solution. The composition of the CMAS precursor was designed to mimic deposits as observed on aircraft turbo shaft shrouds operated in a desert environment [9, 32]. The specific composition was chosen in accordance with prior studies involving the gradient rig test [29, 33], where the composition of a relevant sand sample was analyzed using X-ray fluorescence. The composition of the precursor solution together with the composition of a mixture oxides as resulting from a full transformation is given in Table 1. During testing the specimen’s coated surface was cyclic heated by an open gas burner to a target temperature of 1250°C (above deposit melting temperature) while the back was cooled by pressurized air at the same time. A CMAS glass of similar composition (except from additions of iron, potassium and sodium) was studied by Zaleski et al. where melting temperatures of 1249°C and 1240°C were determined in DSC analysis during succeeding heating cycles [11]. A DTA/TG analysis of the precursor solution dried at 150°C confirmed the decomposition of nitrates in air at temperatures below 1000°C (STA 429 CD, Netzsch, Selb, Germany). Consistently with Zaleski et al., in two subsequent thermal cycles the onset temperature of melting of the mostly glassy deposit was indicated at 1245°C and 1227°C, respectively. Temperatures of surface and back, respectively, were monitored by a long wavelength infrared pyrometer and a thermocouple, respectively. An emissivity of 1 was chosen to evaluate pyrometer readings from the YSZ surface with and without CMAS deposit. This may result in an underestimation of the surface temperature in the range of some ten °C but ensures the surface temperature being beyond melting temperature of the CMAS during the high temperature dwell times. Surface temperature and temperature gradient could be controlled by adapting the fluxes of burner’s fuel and cooling air. At the end of each heating period the burner was moved to a waiting position and the specimen’s surface was cooled by pressured air, too. This additional cooling caused rapid quenching and in some extent an inversed thermal gradient resulting in substantial thermomechanical stresses. Surface and substrate temperatures were continuously logged and average values are given for evaluation in Table 2. Details of the setup are given in Träger et al. [34] and Steinke et al. [28]. Loading parameters as the high temperature dwell time, the concentration, and the injection rate of the CMAS precursor solution were varied. The concentration of the precursor solution was chosen at 0.1 wt% and 0.02 wt%, respectively, while the injection rates was set between 1.2 ml/min and 5 ml/min. Dwell times of heating and cooling were prolonged from the lab standard of 5 minutes of heating and 2 minutes of cooling to ambient temperature (5/2) by a factor of 5 (25/10) and 10 (50/20), respectively. Also test with extensive heating and deposition for more than 180 minutes at a time were conducted where cool down was only initiated eventually when deviations of the surface temperature reading exceeded a surveillance trigger level. Details are listed in Table 2. When significant degradation of the coating, e. g. delamination of the coating close to the bondcoat/TBC interface, was observed the thermal cycling test was stopped.

Phase analysis at the surface level of the ceramic coating after thermal cycling under CMAS was carried out employing X-ray diffraction (XRD) (D4, Bruker AXS GmbH, Karlsruhe, Germany) using Cu Kα radiation. The failure mode and microstructure degradation was investigated on metallographic cross sections by a confocal laser scanning microscope (VK-9710K, Keyence, Japan) and by scanning electron microscopy (SEM) included backscattered electron mode, secondary electron mode, and energy dispersive X-ray spectroscopy (EDS). Devices TM3000 (Hitachi High-Technologies Europe GmbH, Krefeld, Germany) and SEM Ultra 55 (Carl Zeiss NTS GmbH, Oberkochen, Germany), were utilized at intermediate and higher resolutions, respectively. The latter was equipped with a field emission gun (FEG) and an EDS detector of the type INCAEnergy355 (Oxford Instruments PLC, UK).

3 Results and discussion

3.1 Deposition and formation of CMAS by injection of nitrates

In the given experiment CMAS is injected to the combustion flame by means of a mixture of nitrates dissolved in water which also contains nanosized silica from a solid state colloidal sol. This mixture is injected into the center of the flame where the small water droplets are rapidly heated up and water is going to vaporize. The vaporization of water will reduce the volume of the droplets and lead to an increased concentration of the dissolved species while homogeneous mixture on the atomic level is preserved. At the end of this process - taking place within the combustion flame - the CMAS solution is fully dried and reactions between the constituents, similar to the ones observed in a spray pyrolysis process or during precursor plasma spraying, may happen due to the energy available from elevated temperature environment.

On injection the color of the CH_4/O_2 flame is changing in its center from blue to orange. This coloring coincides with the characteristic emission of sodium and calcium atoms. Thereby it can be supposed that at least a part of the dissolved ions have not reacted but stay isolated and get ionized. Following the similarity from the process of spray pyrolysis and taking into account the extent of the colored zone of the flame right to the surface zone of the TBC specimen, it can be anticipated that CMAS and its constituents are reaching the surface of the TBC in a variety of conditions: dissolved at high concentration or as precipitates within a water droplet of reduced volume, in gaseous form caused by evaporation from highly concentrated solution or from disintegration of precipitates, as a solid particle or as fragments of agglomerated precipitates remaining from a fully dried droplet, or as (partly) molten droplet of CMAS.

If the possible conditions during operation of an engine are considered deposits may originate from ingested solid particles, from debris caused by wear or corrosion of earlier engine segments, or from contaminants found in the fuel. Comparing the types of processes in the rig experiment all types of deposition except the case of deposition from the dissolved state may be relevant to the mimic of engine conditions. Each of these conditions implies a different mode and probability of sticking to as well as a specific ability to react with the substrate. To further elucidate which out of the discussed forms is the predominant pathway of CMAS deposition in the burner rig experiment a specimen of YSZ thermal barrier coating has been put in the gradient burner rig with simultaneous CMAS deposition (specimen WDS 2235, details in Table 2). Its surface temperature is kept at a maximum of 1100°C throughout the dwell times which is well below the CMAS melting temperature, so that fusing of the deposits and infiltration into the TBC is not to be expected. Apart from a slight reduction of the overall amount of CH_4/O_2 consumption no change of extend or coloring to the flame is observed and conditions within the flame can be estimated being similar to the case of surface temperatures exceeding the melting temperature of CMAS in the range of 1250°C.

Figure 2a) is showing a SEM image of a cross section prepared from the center of the specimen subjected to CMAS deposition from the combustion flame with surface temperature kept below the melting temperature of CMAS. On the surface a porous and non-continuous deposit of CMAS constituents is found. The cauliflower-like structure is similar to those coating microstructures which are found in spray pyrolysis, suspension plasma spraying (SPS), solution precursor plasma spraying (SPPS) or even plasma-spray physical vapor deposition (PS-PVD) [35-39]. This underlines the similarity to those kinds of processes where deposition and coating formation takes place from submicron scaled particles and clusters or even vapor. Figure 2c) to h) shows EDS elemental mappings at the interface area of substrate and deposit as indicated by the inset rectangle in the cross section of Figure 2a). Mappings for elements of the substrate (zirconium and yttrium) as well as for the constituents of the deposit (calcium, magnesium, aluminum and silicon) are shown, respectively. The distinct distribution of elements Zr and Y on the one hand and Ca and Si on the other hand below and above the interface level, confirms that no infiltration of CMAS into the TBC took place and any reaction at the interface is at a minimum level. An EDS spot analysis within the YSZ layer (Figure 2b)) reveals no indication of CMAS constituents just a few microns below surface level.

A Rietveld evaluation of a X-ray diffraction pattern taken from the surface is shown in Figure 3. Noticeably amount of background intensity flags larger volumes being of amorphous, of low level order or of nanoscaled nature as can be formed due to rapid quenching on the substrate. The missing of splat like structures within the CMAS microstructure indicates the deposition of atoms and nanoscaled agglomerates being the dominant mechanism of deposition. Besides the amorphous background some peaks are observed in the x-ray diffraction pattern which can be attributed to the substrate material of tetragonal YSZ (pattern (a)) or to silicates of melilithe (pattern (b)), and wollastonite type (pattern (c)), respectively. The latter are silicates typically found after crystallization of glasses having a similar composition as the given CMAS mixture. The wollastonite is a rather simple calcium silicon oxide ($CaSiO_3$, space group 2, anorthic) providing also a distinct solubility for e.g. iron. The melilithe is a complex silicate family including a continuous solid-solution series ($Ca_2(Al,Mg)(Si,Al)_2O_7$, space group 113, tetragonal) of calcium aluminum silicate akermanite ($Ca_2Al(AlSi)O_7$) and calcium magnesium silicate gehlenithe ($Ca_2MgSi_2O_7$).

A high-magnification SEM analysis of the CMAS deposit is shown in Figure 4. The inhomogeneous intensity in the image from the backscattered electron detector (BSD) indicates the loss of the atomic scale mixture of the CMAS constituents and the formation of precursors or reaction products throughout the deposition process. Especially the abundance of elements magnesium and aluminum seems to be inhomogeneous (Figure 4c) and d), Figure 2e) and h)) what might be due to their lower concentration on the one hand but may also be fostered by the formation of the melilithe type phases as indicated in X-ray diffraction, on the other hand. Generally, the porous nature confirms the temperature at the surface being below the melting temperature of the CMAS forming oxides. More than this, the cauliflower-like structures are indicative for a particle based deposition mechanism with a diffusion rate too low for the formation of dense crystalline structures. Thereby it can be concluded that the phases found have been formed during in-flight processes or by reactions which require only short diffusion pathways as found in atomic layers or nanoscale clusters. When this kind of formation of CMAS deposit is compared to the above mentioned potential sources of CMAS in turbine engines the burner rig test with simultaneous injection of water based CMAS solutions seems to be well suited to mimic the CMAS attack by sources from gaseous contaminants and sub-micron scaled ingestions or debris.

3.2 CMAS invasion and general attack mechanism in gradient rig testing

Figure 5 shows SEM images of a cross section from specimen WDS 1753 cycled with simultaneous CMAS injection to the combustion flame in the same way as the specimen reported before but at a surface temperature of ca. 1250°C. Under this condition a dense and nearly continuous layer of CMAS deposit is found covering the central area of the TBC surface (Figure 5a) and b)). This CMAS layer can also be seen in further detail in SEM images with high magnification in Figure 6. The dense microstructure indicates that under those process conditions the CMAS deposits of sub-micron microstructure which are condensed from the flame become molten and by fusing are forming the same kind of viscous CMAS layer which would result from droplets originating from larger particles after sticking to the surface.

The different levels of grey from the deposit layer in the BSE images prove the existence of at least to phases being formed from the melt on cooling down from elevated temperatures during test. EDS analyses (e.g. Figure 6d)) indicate that the volumes of dark contrast contain a higher concentration of aluminum and magnesium compared to the areas of light shading, which contain either nearly pure calcium silicate (Figure 6c)) or as well an admixture of zirconium (Figure 6e) and f)). The latter is reasonable in respect to the known dissolution of YSZ into the melt and the potential formation of mixed phases. As for the specimen cycled at lower temperature (WDS2235) the X-ray diffraction pattern taken from the surface of specimens cycled at higher temperatures indicate the presence of YSZ, wollastonite and a melilithe type silicate. Besides this, at some instances reaction products with zirconia as e.g. baghdadite ($Ca_3ZrSi_2O_9$) can be identified. Typically, a number of peaks cannot be attributed unambiguously. This may be related to the small amount, the fine grain size of further phases formed or to the non-equilibrium type of those reaction products.

From the full thickness micrograph of the TBC in it can be seen, that the upper region of the TBC layer appears low porous compared to the microstructure of the TBC layer close to the bond coat interface. Horizontal cracks are formed at different levels of height well above the bond coat interface. As can be seen in Figure 5 infiltration of the porous TBC structure is neither complete nor homogeneous. Filling of large scale porosity is found as well as intrusion in small scale gaps and even into splat boundaries and intra-splat grain boundaries. In Figure 5d) a higher magnification of a typical microstructure at a distance of roughly 100 µm to the surface level is shown ~~together with the EDS elemental mapping of a partly infiltrated region~~. The intrusion in the large scale inter-splat porosity appears sparse and may be limited either by the limited size of some „pore necks“ connecting the open pore network or by the viscosity of the melt which will rise with decreasing temperature along the applied temperature gradient. Unambiguous evidence for the existence of a critical pore radius is difficult to provide as no precise information has been available on the local 3D structure of the pore system. Another note on Figure 5d) is that in the region marked by an ellipse the distinct phases of CMAS are occurring. Thereby, an incongruent melting, indicated by intrusion of only one eutectic composition, is not observed in this study.

The intrusion of CMAS to smaller pores and into the grain boundaries is predominantly observed close to the surface level or in the vicinity of larger amounts of infiltrated CMAS melt. This suggests that this type of intrusion may be a secondary step of the CMAS attack when the reservoir of melt at place is sufficiently high. Where those kind of massively infiltrated regions are located near to the surface and thereby temperature is reasonably high spheroidized fragments and grains of zirconia can be observed which to some extent are completely surrounded by CMAS. This re-shaping of grains and disintegration of TBC splats indicate a high amount of grain boundary diffusion as well as dissolution of YSZ constituents into the melt. This phenomenon is similarly observed in most of the published work on CMAS degradation, common to both, studies of ex-service components and studies under isothermal conditions of intrusion, too, and well described e.g. by Krämer et al. [23]. They also introduced a classification of sublayers within the CMAS penetrated volumes discriminating near-surface regions of highly degraded microstructure from lower level regions where filling of pores has not yet caused disintegration of the original microstructure.

Nevertheless, there is one difference to mention. The formation of spheroidized particles in column gaps of PVD coatings as observed by Krämer et al. [32] is considered of being result of re-precipitation of zirconia from the (saturated) CMAS melt. In the present study, small spherical grains are found within the splat structure, too. Even more important, the formation of larger round shaped grains and the densification of the TBC microstructure is observed in large extent. Thereby the formation of spheroidized grains is not unambiguously the result of re-precipitation but it seems reasonable that the range of mechanism of CMAS interaction is similar to those observed and studied in the application of liquid phase sintering, where processes of diffusion, dissolution, and re-precipitation take place in parallel.

3.3 Mechanical degradation by cycling with/without CMAS

Following the observations of microstructural degradation in the presence of molten CMAS deposits in gradient temperature conditions, their impact on the thermomechanical properties of the TBC layer and the consequences on its strain tolerance, crack growth and the time to failure under cyclic load will be discussed in the following. In Figure 7 macroscopic photographs together with cross sectional micrographs of specimen cycled to failure are shown for specimen tested in the burner rig without ~~(left)~~ and with injection of CMAS ~~(middle and right)~~, respectively. Gradient conditions have been set to temperatures of 1250°C at the TBC surface level and ~1080°C at the bondcoat layer, respectively, for heating dwell times of each 5 minutes followed by 2 minutes of cooling down to temperatures of well below 100°C. Feeding rate of CMAS solution has been ca. 4.5 ml/min with a concentration of constituents set to 0.1wt%.

The type of failure typically observed in the cycling of YSZ coatings in burner rig gradient conditions with moderate thermal load conditions is the formation of a delamination crack close to the bondcoat layer (Figure 7d)). Depending on the interface roughness and the thermal gradient conditions the coalescence of horizontal cracks which are leading to the catastrophic delamination may be formed a little more inwards to the ceramic layer or may be gracing the interface layer including the TGO [40, 41]. This results in delamination of larger parts of the ceramic topcoat at once after an incubation period of usually several hundreds of cycles or tens of hours at high temperature with only a thin layer of TBC residing then on the substrate or even parts of the TGO and bondcoat become bare. The crack growth in this scenario is driven by thermal mismatches between the ceramic TBC layer, the metallic bondcoat layer and the substrate where local stresses even further increase with the formation and growth of the thermally grown oxide (TGO) layer of alumina at the bondcoat-ceramic interface.

In case of the burner rig testing with simultaneous CMAS deposition the type of failure changes dramatically: growth and macroscopic opening of horizontal cracks occurs at several levels within the ceramic layer (Figure 7b) and c)). Cracks with macroscopic crack opening are observed at half coating height and below. Within the upper half more confined cracking partly filled with CMAS is found. This is leading to a spallation of fragments and a progressive chipping of the TBC. This process is regionally and progresses down to the interface level. Overall it results in a non-homogeneously failure where the TGO-bondcoat interface is only covered by a thin layer of remaining TBC and may be bare open at some areas as can be seen in Figure 7b). Changes to the local stress states at the bondcoat interface caused by TGO growth seemingly do not play any role in this scenario.

These observations generally are in accordance with the failure mode which has been deduced from ex-service parts and which have been rationalized in terms of cold shock induced spallation [4, 23]. The CMAS infiltrating the larger voids of the irregular APS microstructure will solidify on cool down and increase Young‘s modulus of the penetrated coating layer and thereby increase the level of strain energy during cool down. Additionally, in regions where CMAS has accessed the (inner) surfaces and grain boundaries of the APS YSZ ceramic coarsening and densification of the splat structure due to enhanced sintering is occurring [42] which also contributes to an increased modulus and potentially increases the fracture toughness in the primarily affected upper TBC layer. The consequences for the growth of delamination cracks within the ceramic layer have been studied in more detail meanwhile [22, 43, 44] and have been summarized as follows: At high cooling rates of the TBC surface a gradient of stress with tension in the upper layer of the ceramic occurs (cold shock conditions). This may result in high peak energy release rates in the early stages of cool down and enables mode I delamination within the ceramic layer. Slower cool down will be dominated by compression in the coating and gives rise to mode II, or near-mode II, delaminations usually close to the bond coat interface. Commonly mentioned by all analyses it is to note, that the presence of vertical separations is a prerequisite for spallation occurring from those delaminations. Those separations may arise from edges, from pre-existing flaws, from sintering cracks, or from channel cracking under extreme cold shock conditions [45].

Actually, as can be seen from Figure 7 or Figure 8, the presence of open vertical cracks could not unambiguously be attested in the present study, although spallation obviously occurred from delamination cracks located within the ceramic layer. Most probably, delamination cracks started from flaws within the irregular microstructure and deflected randomly towards the coating surface. This indicates that the inherent flaws of typical APS coatings are sufficient to allow mode I or near-mode I crack growth. Apart from this, if compared to specimen tested under same thermo-cyclic load but in absence of CMAS, the early occurrence of failure and the vertical position of delamination cracks underline the impact of CMAS on the susceptibility of the coatings to the crack growth under mode I-dominated condition during rapid cool down. Nevertheless, the cool down rate in the present study has not been sufficiently high to trigger channel cracking or major spallation at the very-near surface level in all cases and delaminations cracks are most pronounced in the region close to and below the CMAS infiltrated layer. On repeated thermal cycling the growth, the further opening and the deflection of cracks allows for further infiltration of molten CMAS and also leads to the break-out of lamellae from the coating. As deposition of CMAS continues this results in the observed stepwise chipping of the TBC.

3.4 Impact of different dwell times and deposition rates

In Figure 7 and Figure 8 photographs of specimen after cycling test with continuous CMAS feeding rate of ~4.5 ml/min but different dwell times at elevated temperature of 5 min, 25 min, and 50 min, respectively are shown. All of them commonly show the shallow spallation of TBC throughout nearly the full area of the specimens. From this observation it is reasonable to assume that also the same type of failure mechanism is dominant where the TBC is gradually thinned by breakout of lamellae from the coating surface.

Nevertheless, the number of cycles necessary for the exfoliation to reach the level of the bondcoat interface is systematically changing. The longer the dwell time at elevated temperature and loading with CMAS lasts, the less cycles to failure are observed. This clear trend with spans of more than one order of magnitude is shown in Figure 9. Also shown here is accumulated time at high temperature which is essentially 1:1 correlated with the total amount of CMAS injected for the unchanged feeding conditions. The total time of CMAS exposure until end of life is increasing by roughly 30% only whereas the high temperature dwell time per cycle has been increased more than one order of magnitude. This shows the major role the amount of CMAS is playing to induce crack growth by changing the mechanical properties as compared to an increase of the fatigue loading given by the numbers of cycles.

The trends for the end of life in terms of number of cycles and in terms of total time at high temperature, respectively, keep valid even for dwell times with CMAS deposition of several hours (dashed lines as guide for the eyes in Figure 9). At the same time the macroscopic type of failure is changing dramatically, as can be seen from an example shown in Figure 10. Spallation does not occur at upper and intermediate levels first to cause chipping but large scale delamination within the lower region of the TBC layer is observed. This seems similar to the failure type as known from cycling without CMAS deposits where delamination is found close to the bond coat interface (Figure 7a) and d)). Nevertheless, inspection of cross sections (Figure 10b) and c)) bare differences to the type of degradation discussed before. While the critical spallation happens at low level delaminations similar to the cycling without CMAS at the same time vertical cracks are found as predicted for the cold shock conditions where outer coating layers are stiffened by infiltration of CMAS.

Another variant of failure has been observed when reducing the flux of CMAS constituents as shown in Figure 11. In this experiment the concentration of CMAS constituents in the precursor solution has been reduced by a factor of five whereas the dwell time at high temperature has been five times longer than our reference dwell time of 5 minutes as presented in Figure 7. Overlooking the slight difference in the feeding rates the accumulated load of CMAS deposit per cycle is nearly the same in both experiments but more time is given for infiltration and reaction within the ceramic microstructure. Under these conditions the full set of microscopic degradation modes as depicted from evaluation of ex-service components by Krämer et al. [23] – cold shock channel cracking, spallation at intermediate level of stiffened coating and ultimately delamination at low level near the metallic interface – could be observed coexisting at all. At the same time the type of macroscopic failure could not be unambiguously assigned to surface near spallation or low level delamination, and the times to failure showed an increased scatter, too. Generally, as anticipated, lifetime in terms of time at high temperature considerably increased compared to both experiments with higher CMAS concentration of 0.1wt% for 5 minutes and 25 minutes dwell time, respectively. More interesting, the number of thermal shock cycles until failure has been very similar to the number reached in experiments with shorter dwell times.

The apparent discrepancy from the proposed sequence of degradation [23] may be unraveled when both the current experimental setup and the boundary conditions used in the mechanical analysis so far are being considered. From the studies performed at isothermal reference conditions it is known that at relevant temperatures the infiltration of a deposited CMAS layer takes place on rather short time scales. It is reasonable at that point to assume that e.g. under aeronautic service conditions which comprise high temperature dwell times of several hours the molten CMAS deposits will readily infiltrate down to a level limited by the temperature of solidification. Consistently, mechanical modelling of coating delamination so far considers stresses evolving from thermal gradient conditions as well as from local temperature evolution at transient conditions but not yet reflects a protracted degradation of coating microstructure and mechanical properties as a consequence of CMAS attack.

The influence of the kinetics of CMAS intrusion may be considered as follows: Viscosity of the model CMAS used in this study can be calculated with the empirical approach published by Fluegel [46]. Predicted values for the relevant temperature range of burner rig test are 10 Pa·s, 100 Pa·s, and 1000 Pa·s at 1264°C, 1130°C, and 1035°C, respectively. With reference to the discussion by Krämer et al. [32] the viscosity of the glass at 1250°C should be thereby low enough to allow infiltration of micrometer scaled porosity close to the surface level within a time scale of a few minutes. Adopting this model of infiltration kinetics at isothermal conditions, given for a capillary having a 1 µm diameter, one can roughly estimate the time necessary to infiltrate open porosity down to a level of lower temperature. Considering temperature distribution in the given series of lifetime tests as calculated from the one dimensional heat flux approximation, a temperature of 1130°C is reached ca. 300 µm below surface level. The time to reach this level would be in the order of one hour what by order or magnitude is consistent with the length of dwell times were low level delamination has been dominantly occurring.

In this burner rig study two more aspects are altered: first, the CMAS deposit has been steadily supplied at limited rate, second, thermal shock has been applied cyclic with dwell times being relatively short in most tests. Accordingly, at least at the beginning of each test the infiltration depth of CMAS may be controlled by the amount presently available. Additionally, the stresses evolving from repeated thermal shock of the coatings with continuously changing mechanical properties allow for a multiplicity of cracks forming at various levels in the course of the test. Thereby, the coexistence and presumable competitive growth of cracks in different coating levels may be one reason for the increase of stochastic scatter observed not only in terms of failure mode but also in terms of the time to failure.

Although the progressive character of degradation under the given test conditions complicates the direct link to the modelling results, there are some indicative trends to highlight. With longer dwell times throughout the experimental series the regions of most pronounced delamination cracks have been shifting closer to the interface where no indications of CMAS infiltration have been observed. The formation of channel cracks and branching of surface near spallation cracks has only been found where long-term dwell times allowed CMAS to penetrate larger coating volumes without interference of thermal shock events. The chipping of infiltrated surface layers can easily be understood in terms of the available strain energy which is increasing with the thickness and the elastic modulus of the infiltrated and densified layer. The trend of the position of cracking, mentioned first, is providing strong indication that the infiltrated layer is not only stiffened, but may also evolve an increased fracture toughness compared to the original coating. This is probably due to an enhancement of inter-splat bonding induced by the CMAS supported sintering [42].

At that point it is interesting to note that for all tests the accumulated amount of CMAS precursors which has been sprayed towards the specimen surface in first proximity is invariant at time of failure (Figure 12). This observation may underpin the picture where liquid CMAS is successively filling up the open porosity of a coating from its surface level as much as CMAS is available and where the coating is thinning down by piece-wise spallation of infiltrated lamellae whenever at cool down the strain energy of the stiffened outer volume exceeds the critical energy release rate of the ceramic. Actually, there are arguments that this may be oversimplified: First, strain release due to multi-level cracking or opening of channel cracks is not reflected in this simple picture. Second, in this setup the amount of CMAS oxide which is available to infiltrate porosity is not one-to-one linked with the amount of precursors injected into the flame. A rough estimation yields a volume of CMAS potentially condensing from the atomized solution of more than twice the volume of open porosity of the coating (ca 0.4 g of CMAS oxides formed from 1 g of precursors, specific density of CMAS glass below 3 g/cm^3 [10, 19], 17% open porosity at 450 µm coating thickness, ca. 7 cm^2 specimen surface area). Even more, microstructural characterization clearly proved the inhomogeneous nature of the sparse CMAS intrusion and volume increase due to buckling has not been observed to explain this discrepancy. This indicates that only a fraction of less than 50% of the injected CMAS precursors condensed on the specimen surface and some amount is transported with the combustion gas stream to other places within the rig or to the exhaust. A similar order of magnitude can be estimated when the scale thickness of the non-molten deposit on specimen WDS2235 (section 3.1) is considered. Restricted onto the surface area of the specimen, the injection rate of CMAS solution of 1.2 ml/min at a concentration of 0.1wt.% after 250 minutes (50x 5 minutes) would add up to a loading with CMAS oxides of ca. 15mg/cm^2. If we compare this with the loading derived from the scale thickness of ca 20µm in Figure 2a) which equals to 6 mg/cm^2 (density as above), we end up with a deposition efficiency of 40% (or 20%, if we reflect the porous nature of the deposit).

At all, the reproducibility of experimental lifetimes and the steady shift of the spallation depth observed give rise to the assumption that condensation of CMAS takes place at a rate in first order proportional to the available feed and that infiltration results in a systematic layer-wise degradation of at least averaged mechanical properties. From this, one can suggest to specify the maximum allowable time of operation for a gas turbine at a known concentration of CMAS in the combustion atmosphere by the critical value of the product of concentration and time at operation. To derive such a maximum permissible value from the given experiment first we need the mass flow rate of the combustion gas, which can be calculated from the gas mixture used to operate the burner rig. For a typical mixture of CH_4 and O_2 used in this study this sums up to ca 36 g/min of H_2O, CO_2, and O_2, including the vaporized water arising from the solution of precursors. With the feed rate of the precursor solution of e.g. 0.1wt% at 4.5 ml/min we find a load of contaminants equivalent to 1.8 mg/min of CMAS oxides carried with the combustion gas what can be expressed as a concentration of 50 ppm. Considering the corresponding time to failure of 4-7 hours a lower threshold value would be ca. 200 ppm·h, indicating that at a CMAS concentration of only 1 ppm the allowable time of operation could be increased to 200 hours.

Obviously, conditions in a gas turbine, as e.g. the total pressure, temperatures, and sources of contaminants will be diverse compared to this lab scale experiment. Parameters like varying CMAS compositions, particle size distributions, angle of particle incidence and a lot further more would need to be considered to reliably model the accumulation of CMAS on the TBC surface. Nevertheless, it can be concluded that contaminant levels in the range of ppm should be recognized as critical in respect to degradation by CMAS and the criterion of a maximum permissible value for the product of concentration and time at operation can be a practical approach for the definition of safety rules for this type of attack.

4 Summary and conclusion

The test of TBCs in thermal gradient conditions on a burner rig with simultaneous CMAS injection proves to simulate load conditions in a proper way to reproduce major observations of degradation modes of ex-service airfoils inspected after subjected to CMAS attack. Degradation of microstructure like filling up of porosity, the dissolution of YSZ ceramic to the melt, densification of the TBC, and the formation of cracks at different locations within the ceramic layer are observed. As the reservoir of molten CMAS is formed right at the surface level load scenarios from a large variety of potential CMAS sources ranging from ingested solid particles to gaseous contaminants can be simulated. The similarity of degradation modes and the observation that the totalized amount of CMAS is the most significant parameter in respect to the spallation lifetime underline the impact of CMAS to the health of coatings. This consequence is to be considered even at very low deposition rates and a maximum permissible amount can be a practical approach for the definition of safety rules for this type of attack. The questions, if a nonhazardous concentration of CMAS can be defined, or what is the consequence of multiple non-continuous loading with CMAS deposits, may motivate further investigations.

The full set of microscopic degradation modes reported and rationalized in earlier studies could be observed. However, the dominant path to failure under the thermo-cyclic loading in this study has been delamination cracking within the ceramic just underneath the CMAS affected layer. On continued cycling and CMAS deposition new surfaces and unaffected volumes are exposed and infiltrated in a step by step process what results in a progressive exfoliation. Channel cracking and surface near branching of cracks could only be observed for rather long dwell times were large amounts of CMAS could intrude and stiffen regions of the coating well below the surface near region. This can be understood when both, the increase of elastic modulus as well as of fracture toughness in the infiltrated layers is taken into account.

Obviously, an improved tolerance against spallation under CMAS attack will be obtained if the strain energy stored in the infiltrated layer can be lowered. This is commonly aimed by applying top layer materials which can limit the infiltration depth to a minimum. The observations made in this study on the concurrent degradation modes additionally indicate that e.g. the proportion of fracture toughness between affected and unaffected layer, respectively, will have an impact on time and mode of spallation. This is where an adaption of microstructures can further support the optimization strategy. For a deeper understanding one will need to consider the particular kinetics of pore filling, sintering, and disintegration induced by CMAS and their specific relevance for the evolution of mechanical properties of the porous ceramic.

Acknowledgements

The authors gratefully acknowledge the invaluable support of further colleagues at Forschungszentrum Jülich GmbH~~ (IEK-1)~~: Mr. Karl-Heinz Rauwald and Mr. Ralf Laufs for manufacturing of coatings, Mrs. Sigrid Schwarz-Lückge for conducting mercury intrusion tests of free standing coatings, Dr. Dietmar Kobertz for DTA/TG-analysis of CMAS feedstock, Mrs. Nicole Adels for support in performing the burner rig tests, Mrs. Roxana Hintzen for producing high quality cross sectional laser scanning micrographs, and Mrs. Yoo Jung Sohn and Mrs. Caren Gatzen for contributions to the evaluation of XRD pattern.

References

1. Miller, R., *Thermal barrier coatings for aircraft engines: history and directions.* Journal of Thermal Spray Technology, 1997. **6**(1): p. 35-42.

2. Darolia, R., *Thermal barrier coatings technology: critical review, progress update, remaining challenges and prospects.* International Materials Reviews, 2013. **58**(6): p. 315-348.

3. de Wet, D.J., R. Taylor, and F.H. Stott, *Corrosion mechanisms of ZrO2-Y2O3 thermal barrier coatings in the presence of molten middle-east sand.* J. Phys., 1993. **3**: p. 655.

4. Mercer, C., S. Faulhaber, A.G. Evans, and R. Darolia, *A delamination mechanism for thermal barrier coatings subject to calcium-magnesium-alumino-silicate (CMAS) infiltration.* Acta Materialia, 2005. **53**(4): p. 1029-1039.

5. Smialek, J., F. Archer, and R. Garlick, *Turbine airfoil degradation in the persian gulf war.* JOM, 1994. **46**(12): p. 39-41.

6. Levi, C.G., J.W. Hutchinson, M.H. Vidal-Sétif, and C.A. Johnson, *Environmental degradation of thermal-barrier coatings by molten deposits.* MRS Bulletin, 2012. **37**(10): p. 932-941.

7. Wellman, R.G. and J.R. Nicholls, *Erosion, corrosion and erosion–corrosion of EB PVD thermal barrier coatings.* Tribology International, 2008. **41**(7): p. 657-662.

8. Strangman, T., D. Raybould, A. Jameel, and W. Baker, *Damage mechanisms, life prediction, and development of EB-PVD thermal barrier coatings for turbine airfoils.* Surface and Coatings Technology, 2007. **202**(4-7): p. 658-664.

9. Borom, M.P., C.A. Johnson, and L.A. Peluso, *Role of environmental deposits and operating surface temperature in spallation of air plasma sprayed thermal barrier coatings.* Surface and Coatings Technology, 1996. **86-87**(PART 1): p. 116-126.

10. Bansal, N.P. and S.R. Choi, *Properties of CMAS glass from desert sand.* Ceramics International, 2015. **41**(3, Part A): p. 3901-3909.

11. Zaleski, E.M., C. Ensslen, C.G. Levi, and D. Butt, *Melting and Crystallization of Silicate Systems Relevant to Thermal Barrier Coating Damage.* Journal of the American Ceramic Society, 2015. **98**(5): p. 1642-1649.

12. van Dyk, J.C., F.B. Waanders, S.A. Benson, M.L. Laumb, and K. Hack, *Viscosity predictions of the slag composition of gasified coal, utilizing FactSage equilibrium modelling.* Fuel, 2009. **88**(1): p. 67-74.

13. Wiesner, V.L., U.K. Vempati, and N.P. Bansal, *High temperature viscosity of calcium-magnesium-aluminosilicate glass from synthetic sand.* Scripta Materialia, 2016. **124**: p. 189-192.

14. Wellman, R., G. Whitman, and J.R. Nicholls, *CMAS corrosion of EB PVD TBCs: Identifying the minimum level to initiate damage.* International Journal of Refractory Metals and Hard Materials, 2010. **28**(1): p. 124-132.

15. Braue, W., *Environmental stability of the YSZ layer and the YSZ/TGO interface of an in-service EB-PVD coated high-pressure turbine blade.* Journal of Materials Science, 2009. **44**(7): p. 1664-1675.

16. Witz, G., V. Shklover, W. Steurer, S. Bachegowda, and H.P. Bossmann, *High-temperature interaction of yttria stabilized zirconia coatings with CaO–MgO–Al2O3–SiO2 (CMAS) deposits.* Surface and Coatings Technology, 2015. **265**(0): p. 244-249.

17. Li, L. and D.R. Clarke, *Effect of CMAS Infiltration on Radiative Transport Through an EB-PVD Thermal Barrier Coating.* International Journal of Applied Ceramic Technology, 2008. **5**(3): p. 278-288.

18. Wiesner, V.L. and N.P. Bansal, *Crystallization kinetics of calcium–magnesium aluminosilicate (CMAS) glass.* Surface and Coatings Technology, 2014. **259, Part C**: p. 608-615.

19. Wiesner, V.L. and N.P. Bansal, *Mechanical and thermal properties of calcium–magnesium aluminosilicate (CMAS) glass.* Journal of the European Ceramic Society, 2015. **35**(10): p. 2907-2914.

20. Braue, W. and P. Mechnich, *Recession of an EB-PVDYSZ Coated Turbine Blade by CaSO4 and Fe, Ti-Rich CMAS-Type Deposits.* Journal of the American Ceramic Society, 2011. **94**(12): p. 4483-4489.

21. Hutchinson, J.W. and A.G. Evans, *On the delamination of thermal barrier coatings in a thermal gradient.* Surface and Coatings Technology, 2002. **149**(2–3): p. 179-184.

22. Evans, A.G. and J.W. Hutchinson, *The mechanics of coating delamination in thermal gradients.* Surface and Coatings Technology, 2007. **201**(18): p. 7905-7916.

23. Krämer, S., S. Faulhaber, M. Chambers, D.R. Clarke, C.G. Levi, J.W. Hutchinson, and A.G. Evans, *Mechanisms of cracking and delamination within thick thermal barrier systems in aero-engines subject to calcium-magnesium-alumino-silicate (CMAS) penetration.* Materials Science and Engineering: A, 2008. **490**(1-2): p. 26-35.

24. Gell, M., L. Xie, E.H. Jordan, and N.P. Padture, *Mechanisms of spallation of solution precursor plasma spray thermal barrier coatings.* Surface and Coatings Technology, 2004. **188–189**: p. 101-106.

25. Shan, X., Z. Zou, L. Gu, L. Yang, F. Guo, X. Zhao, and P. Xiao, *Buckling failure in air-plasma sprayed thermal barrier coatings induced by molten silicate attack.* Scripta Materialia, 2016. **113**: p. 71-74.

26. Begley, M.R., LayerSlayer: An Open Source Code for Analyzing Multilayers, 2012.

27. Shinozaki, M., K.A. Roberts, B. Van De Goor, and T. William Clyne, *Deposition of ingested volcanic ash on surfaces in the turbine of a small jet engine.* Advanced Engineering Materials, 2013. **15**(10): p. 986-994.

28. Steinke, T., D. Sebold, D.E. Mack, R. Vaßen, and D. Stöver, *A novel test approach for plasma-sprayed coatings tested simultaneously under CMAS and thermal gradient cycling conditions.* Surface and Coatings Technology, 2010. **205**(7): p. 2287-2295.

29. Drexler, J.M., A. Aygun, D. Li, R. Vaßen, T. Steinke, and N.P. Padture, *Thermal-gradient testing of thermal barrier coatings under simultaneous attack by molten glassy deposits and its mitigation.* Surface and Coatings Technology, 2010. **204**(16-17): p. 2683-2688.

30. Steinke, T., M.O. Jarligo, D.E. Mack, R. Vassen, and D. Stoever, *The influence of CMAS attack on the lifetime of thermal barrier coatings.* DVS-Ber., 2011. **276**(Copyright (C) 2012 American Chemical Society (ACS). All Rights Reserved.): p. a190/1-a190/6.

31. Jackson, R.W., E.M. Zaleski, D.L. Poerschke, B.T. Hazel, M.R. Begley, and C.G. Levi, *Interaction of molten silicates with thermal barrier coatings under temperature gradients.* Acta Materialia, 2015. **89**(0): p. 396-407.

32. Krämer, S., J. Yang, C.G. Levi, and C.A. Johnson, *Thermochemical Interaction of Thermal Barrier Coatings with Molten CaO-MgO-Al2O3-SiO2 (CMAS) Deposits.* Journal of the American Ceramic Society, 2006. **89**(10): p. 3167-3175.

33. Aygun, A., A.L. Vasiliev, N.P. Padture, and X. Ma, *Novel thermal barrier coatings that are resistant to high-temperature attack by glassy deposits.* Acta Materialia, 2007. **55**(20): p. 6734-6745.

34. Traeger, F., R. Vassen, K.H. Rauwald, and D. Stöver, *Thermal cycling setup for testing thermal barrier coatings.* Advanced Engineering Materials, 2003. **5**(6): p. 429-433.

35. Perednis, D., O. Wilhelm, S.E. Pratsinis, and L.J. Gauckler, *Morphology and deposition of thin yttria-stabilized zirconia films using spray pyrolysis.* Thin Solid Films, 2005. **474**(1–2): p. 84-95.

36. Beckel, D., D. Briand, A.R. Studart, N.F. de Rooij, and L.J. Gauckler, *Topography Mediated Patterning of Inorganic Materials by Spray Pyrolysis.* Advanced Materials, 2006. **18**(22): p. 3015-3018.

37. Padture, N.P., K.W. Schlichting, T. Bhatia, A. Ozturk, B. Cetegen, E.H. Jordan, M. Gell, S. Jiang, T.D. Xiao, P.R. Strutt, E. Garcia, P. Miranzo, and M.I. Osendi, *Towards durable thermal barrier coatings with novel microstructures deposited by solution-precursor plasma spray.* Acta Materialia, 2001. **49**(12): p. 2251-2257.

38. Kassner, H., R. Siegert, D. Hathiramani, R. Vassen, and D. Stoever, *Application of Suspension Plasma Spraying (SPS) for Manufacture of Ceramic Coatings.* Journal of Thermal Spray Technology, 2008. **17**(1): p. 115-123.

39. Hospach, A., G. Mauer, R. Vaen, and D. Stöver, *Columnar-structured thermal barrier coatings (TBCs) by thin film low-pressure plasma spraying (LPPS-TF).* Journal of Thermal Spray Technology, 2011. **20**(1-2): p. 116-120.

40. Trunova, O., T. Beck, R. Herzog, R.W. Steinbrech, and L. Singheiser, *Damage mechanisms and lifetime behavior of plasma sprayed thermal barrier coating systems for gas turbines--Part I: Experiments.* Surface and Coatings Technology, 2008. **202**(20): p. 5027-5032.

41. Nordhorn, C., R. Mucke, K.A. Unocic, M.J. Lance, B.A. Pint, and R. Vassen, *Effects of thermal cycling parameters on residual stresses in alumina scales of CoNiCrAlY and NiCoCrAlY bond coats.* Surface & Coatings Technology, 2014. **258**: p. 608-614.

42. Shinozaki, M. and T.W. Clyne, *The effect of vermiculite on the degradation and spallation of plasma sprayed thermal barrier coatings.* Surface and Coatings Technology, 2013. **216**(0): p. 172-177.

43. Sundaram, S., D.M. Lipkin, C.A. Johnson, and J.W. Hutchinson, *The Influence of Transient Thermal Gradients and Substrate Constraint on Delamination of Thermal Barrier Coatings.* Journal of Applied Mechanics, 2012. **80**(1): p. 011002-011002.

44. Jackson, R.W. and M.R. Begley, *Critical cooling rates to avoid transient-driven cracking in thermal barrier coating (TBC) systems.* International Journal of Solids and Structures, 2014. **51**(6): p. 1364-1374.

45. Zhao, L.G., T.J. Lu, and N.A. Fleck, *Crack channelling and spalling in a plate due to thermal shock loading.* Journal of the Mechanics and Physics of Solids, 2000. **48**(5): p. 867-897.

46. Fluegel, A., *Glass viscosity calculation based on a global statistical modelling approach.* Glass Technology-European Journal of Glass Science and Technology Part A, 2007. **48**(1): p. 13-30.

Table 1:

Table 1: Composition of the precursor solution in accordance to [28]. The precursor solution has been diluted in distilled water down to an overall concentration of 0.1wt% or 0.02wt%, respectively. Also given is the composition of the oxide mixture resulting from a full transformation of precursors.

Component (precursor form)	Fraction in mol%	Component (oxide form)	Fraction in mol%	Fraction in wt%
Colloidal silica (SiO_2)	50	SiO2	52.8	52.4
$Ca(NO_3)_2 \cdot 4H_2O$	38	CaO	39.4	37.2
$Mg(NO_3)_2 \cdot 6H_2O$	5	MgO	5.2	3.5
$Al(NO_3)_3 \cdot 9H_2O$	4	Al2O3	2.1	3.6
$NaNO_3$	1	Na2O5	0.5	0.5
KNO_3	1	K2O	0.5	1.4
$Fe(NO_3)_3 \cdot 9H_2O$	1	Fe2O3	0.5	1.4

Table 2:

Table 2: Test conditions and spallation lifetimes of YSZ TBCs in gradient burner rig cycling with simultaneous injection of CMAS precursor solution (* WDS2235 unfailed, for ageing only; average temperatures with standard deviation)

Specimen (Label)	Feed rate of solution in ml/min	Concentration of solution in wt%	Dwell time at high temp. in min	Avg. surface temperature in °C (SD)	Avg. substrate temperature in °C (SD)	Total number of cycles
WDS 1753	1.2	0.1	5	1259 (26)	1047 (28)	177
WDS 2235	1.2	0.1	5	970 (36)	812 (29)	(50)*
WDS 2275	n.a.	n.a.	5	1239 (26)	1018 (31)	2801
WDS 2279	4.5	0.1	5	1209 (52)	1030 (54)	49
WDS 2280	4.5	0.1	5	1234 (28)	1040 (27)	50
WDS 2281	4.5	0.1	25	1222 (42)	1055 (10)	11
WDS 2282	4.5	0.1	25	1205 (45)	1055 (25)	13
WDS 2283	4.5	0.1	50	1222 (53)	1057 (15)	5
WDS 2284	4.5	0.1	50	1222 (23)	1056 (12)	3
WDS 2285	5.0	0.1	>180	1237 (45)	1064 (20)	2
WDS 2286	5.0	0.1	>210	1242 (37)	1052 (20)	2
WDS 2287	4.0	0.02	25	1239 (43)	1030 (28)	56
WDS 2288	4.0	0.02	25	1225 (25)	1052 (17)	37

Figure Captions

Figure 1: Photograph of a specimen under test in the burner rig with simultaneous injection of the CMAS solution. The orange coloring indicates atomic emission spectra of dissolved CMAS constituents.

Figure 2: SEM analysis results collected from the center of a specimen subjected to CMAS deposition from the combustion flame with surface temperatures kept below the melting temperature of the deposit: a) SEM image ~~(upper left)~~ taken from a polished cross section with position marker of EDS spot analysis, b) EDS result, c) to h) EDS intensity pattern for relevant species.~~ (lower row, inset in SEM image marks area of EDS analysis) and x-ray diffraction pattern taken from the surface level prior to embedding~~

Figure 3: Rietveld refinement of an X-ray diffraction pattern taken from the surface of a sample subjected to CMAS deposition from the combustion flame with surface temperatures kept below the melting temperature of the deposit. Bragg pattern: (a) Yttria-stabilized zirconia, (b) Akermanite-gehlenite, (c) Wollastonite (anorthic).

Figure 4: High-magnification SEM images and EDS spot analyses of CMAS deposit kept below the melting temperature: a) SEM image with backscattered electron contrast, b) SEM image with in-lens contrast, c)-d) EDS results at indicated positions (1) and (2).

Figure 5: SEM images taken from the cross section of a typical plasma sprayed porous YSZ coating after deterioration by CMAS attack in the gradient burner rig: a) surface near region, b) surface layer, c) overview at full coating height, d) open crack region.

Figure 6: SEM analyses from the surface near region of a deteriorated APS coating - same cross section as shown in Figure 5: a,b) SEM micrographs with position markers (1-4) of EDS spot analyses, c-d) EDS results.

Figure 7: Macroscopic photographs (upper row) together with cross sectional micrographs (lower row) of specimen cycled to failure at reference cycling conditions (5 minutes heating, 2 minutes cooling with temperatures during heating dwell time of ~1250°C at surface level and ~1080°C at the bondcoat layer): (a/d) without and (b/e,c/f) with simultaneous injection of ~4.5 ml/min CMAS solutions of concentration 0.1wt% .

Figure 8: Macroscopic photographs (left) together with cross sectional micrographs of specimen cycled to failure with simultaneous injection of ~4.5ml/min CMAS solutions of concentration 0.1wt% with dwell times at high temperature per cycle of (a-c) 25 minutes and (d-f) 50 minutes.

Figure 9: Number of thermal cycles (circles) and the total time at high temperature (diamond) at time of failure of APS YSZ TBC specimen vs hot dwell time per thermal cycle in burner rig test with continuous injection of CMAS solution. Closed symbols represent specimen loaded with a CMAS flux of ~4.5 ml/min at 0.1wt%, open symbols are attributed to specimen with lower flux of ~4 ml/min at 0.02wt%. Dashed lines for guidance only.

Figure 10: Macroscopic photograph (a) and cross sectional micrographs (b,c) of specimen cycled to failure with simultaneous injection of ~4.5ml/min CMAS solutions of concentration 0.1wt% with dwell times of approx. 3 hours.

Figure 11: Macroscopic photographs (a,d) together with cross sectional micrographs (b/c,e/f) of specimens cycled to failure with a CMAS flux of ~4 ml/min at 0.02wt%.and 25min dwell times at high temperature.

Figure 12: Accumulated amount of CMAS precursors at time of failure of APS YSZ TBC specimen which have been continuously atomized into the flame in burner rig test. Closed symbols represent specimen loaded with a flux of CMAS precursors of ~5 mg/min, open symbols are attributed to specimen with lower flux of 0,8 mg/min.

Figure 1:

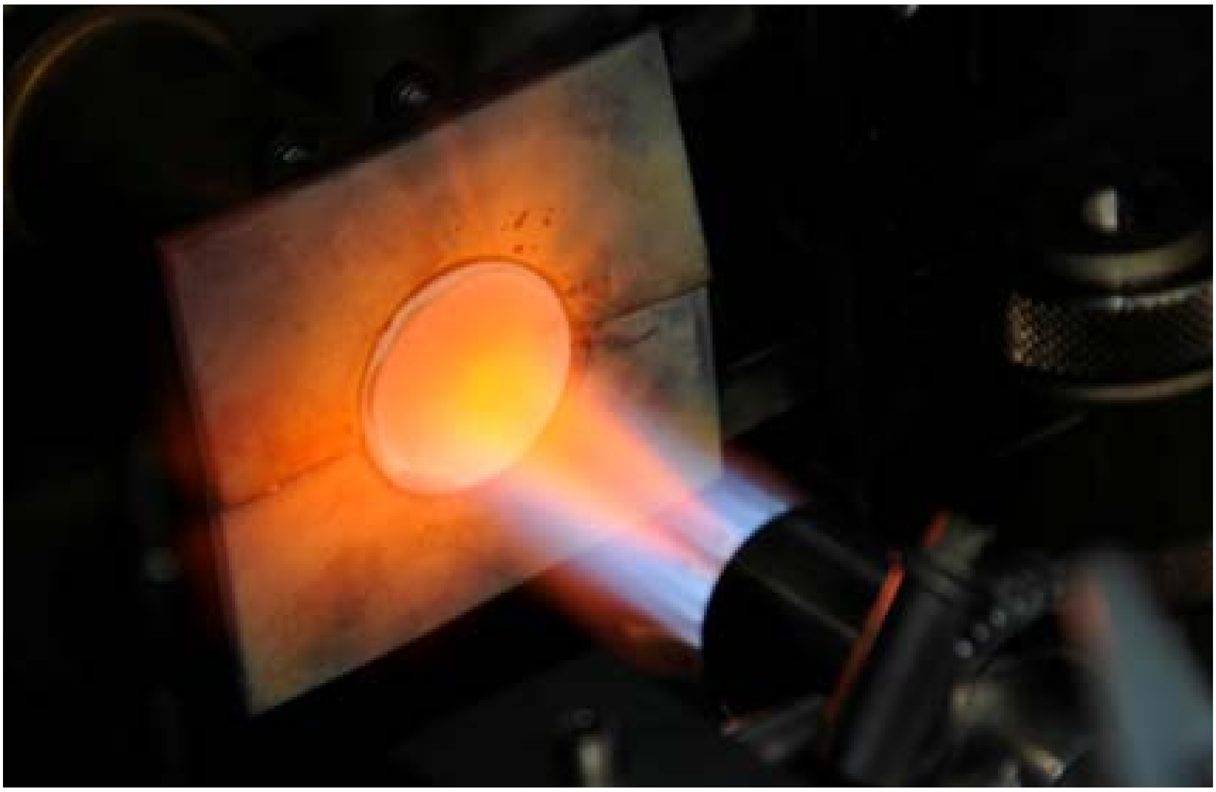

Figure 2: (updated, split)

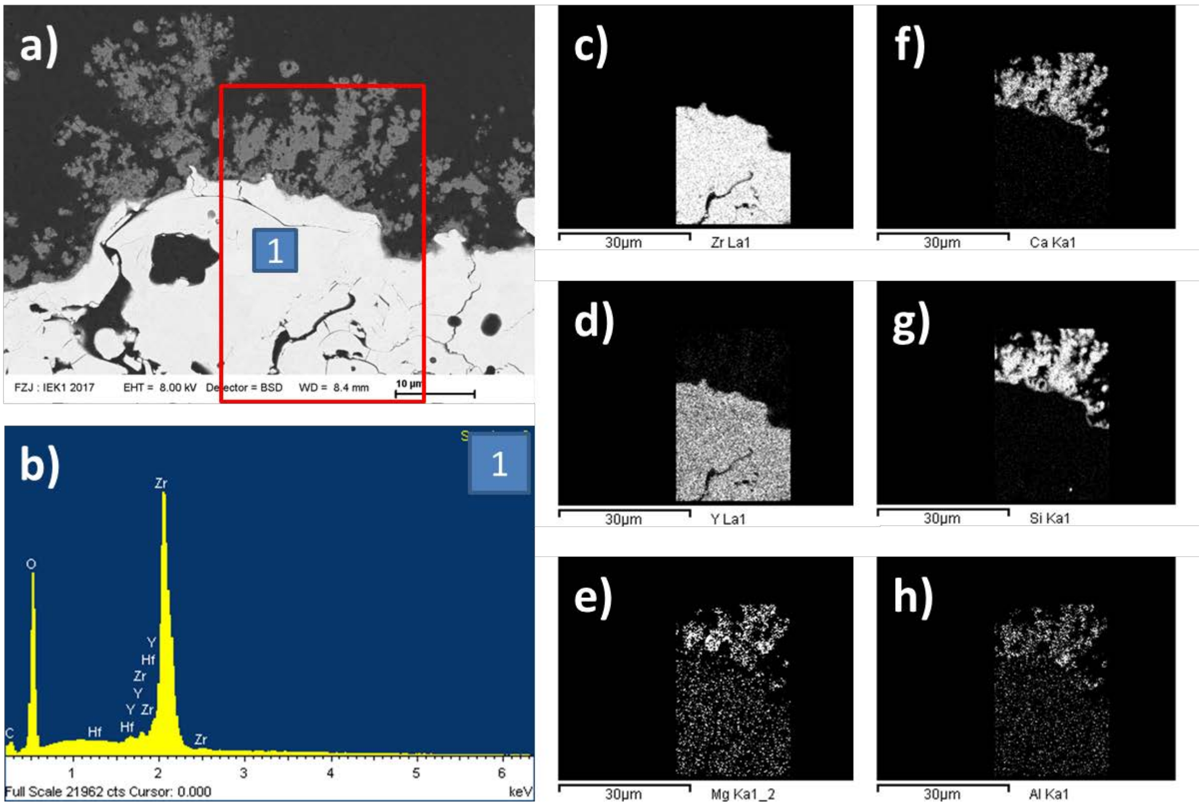

Figure 3: (new, prior part of Figure 2)

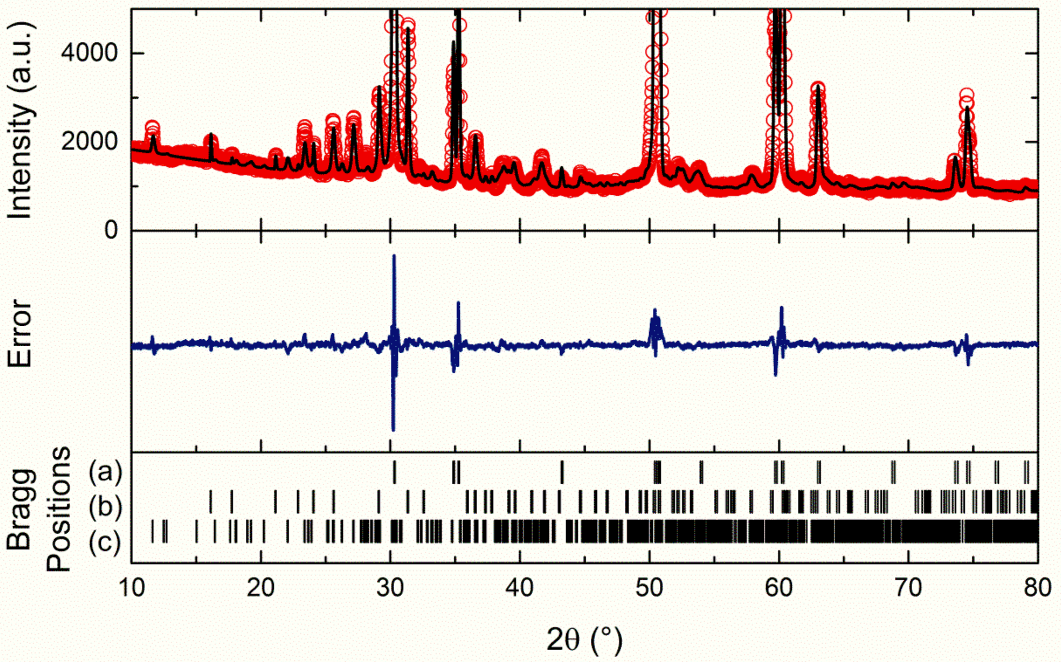

Figure 4: (new)

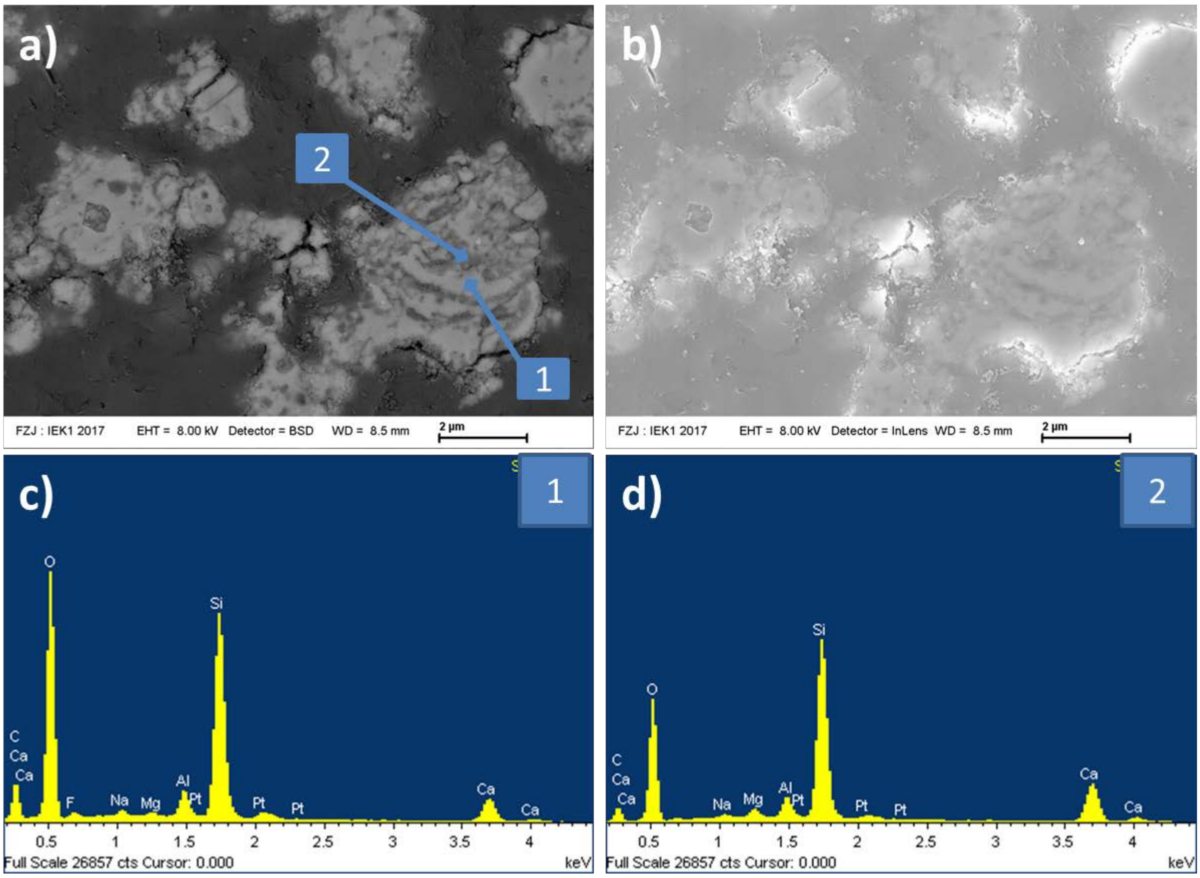
a)
2
1
FZJ : IEK1 2017 EHT = 8.00 kV Detector = BSD WD = 8.5 mm
2 µm
b)
FZJ : IEK1 2017 EHT = 8.00 kV Detector = InLens WD = 8.5 mm
2 µm
c)
1
O
Si
C
Ca
Ca
F
Na
Mg
Al
Pt
Pt
Pt
Ca
Ca
0.5
1
1.5
2
2.5
3
3.5
4
Full Scale 26857 cts Cursor: 0.000
keV
d)
2
Si
O
C
Ca
Ca
Na
Mg
Al
Pt
Pt
Pt
Ca
Ca
0.5
1
1.5
2
2.5
3
3.5
4
Full Scale 26857 cts Cursor: 0.000
keV

Figure 5: (merged from prior Figure 3 and Figure 4 and Figure 5)

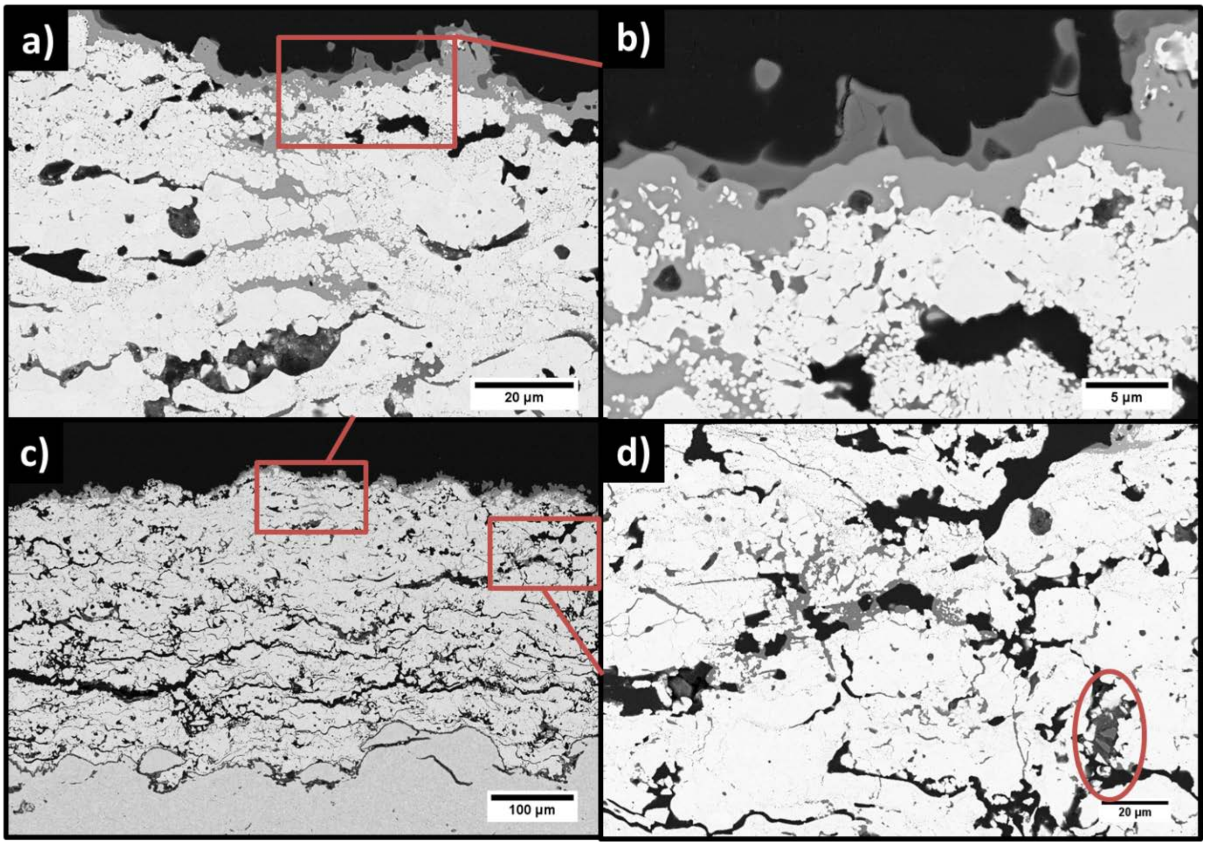

Figure 6: (new)

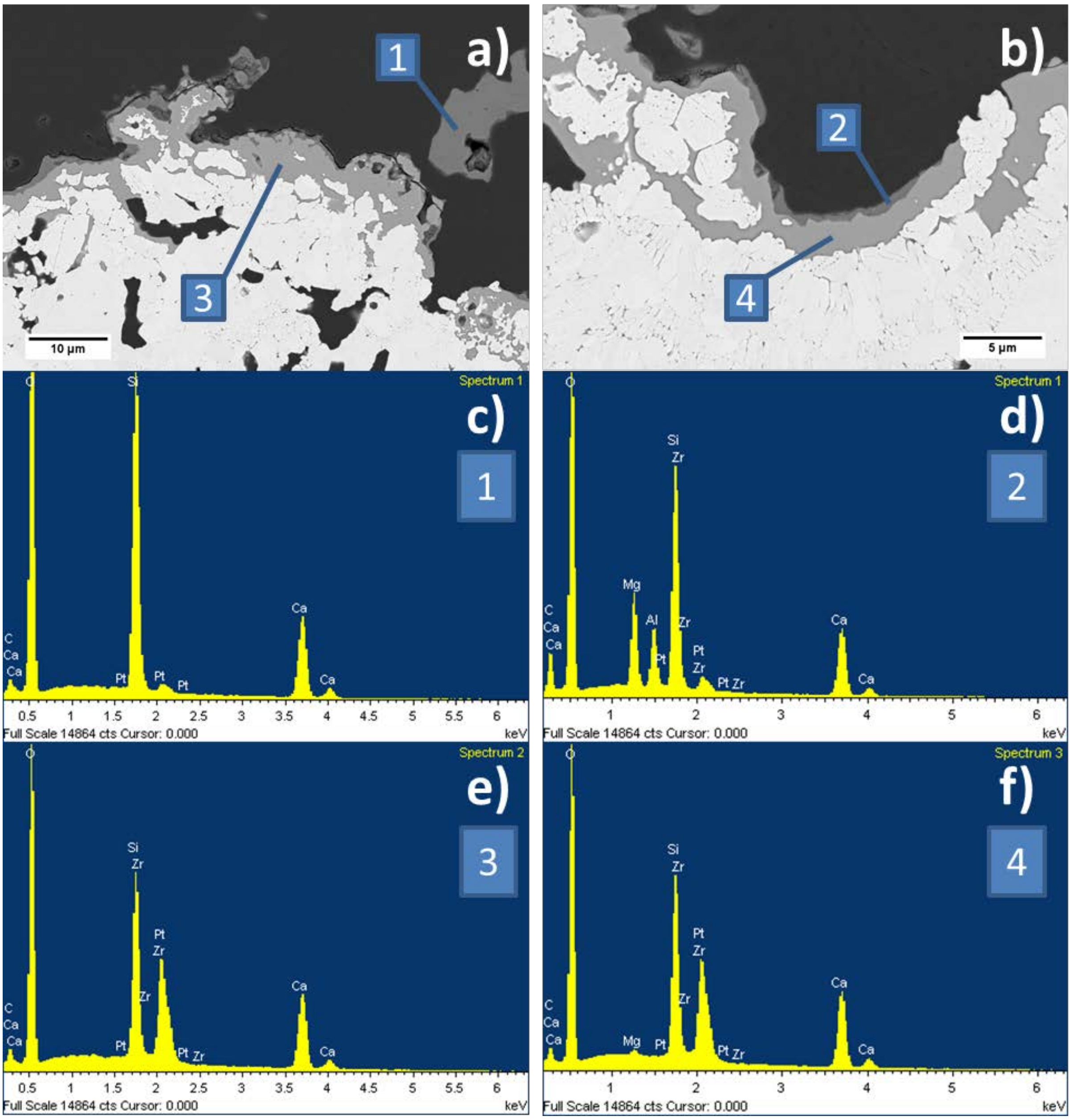
a)
1
3
10 µm
b)
2
4
5 µm
c)
1
Spectrum 1
O
Si
C
Ca
Ca
Pt
Pt
Pt
Ca
Ca
0.5 1 1.5 2 2.5 3 3.5 4 4.5 5 5.5 6
Full Scale 14864 cts Cursor: 0.000
keV
d)
2
Spectrum 1
O
Si
Zr
Mg
Al
Pt
Zr
Pt
Zr
Pt Zr
C
Ca
Ca
Ca
Ca
1 2 3 4 5 6
Full Scale 14864 cts Cursor: 0.000
keV
e)
3
Spectrum 2
O
Si
Zr
Pt
Zr
Zr
Pt
Pt Zr
C
Ca
Ca
Ca
Ca
0.5 1 1.5 2 2.5 3 3.5 4 4.5 5 5.5 6
Full Scale 14864 cts Cursor: 0.000
keV
f)
4
Spectrum 3
O
Si
Zr
Pt
Zr
Zr
Mg
Pt
Pt Zr
C
Ca
Ca
Ca
Ca
1 2 3 4 5 6
Full Scale 14864 cts Cursor: 0.000
keV

Figure 7: (prior Figure 6)

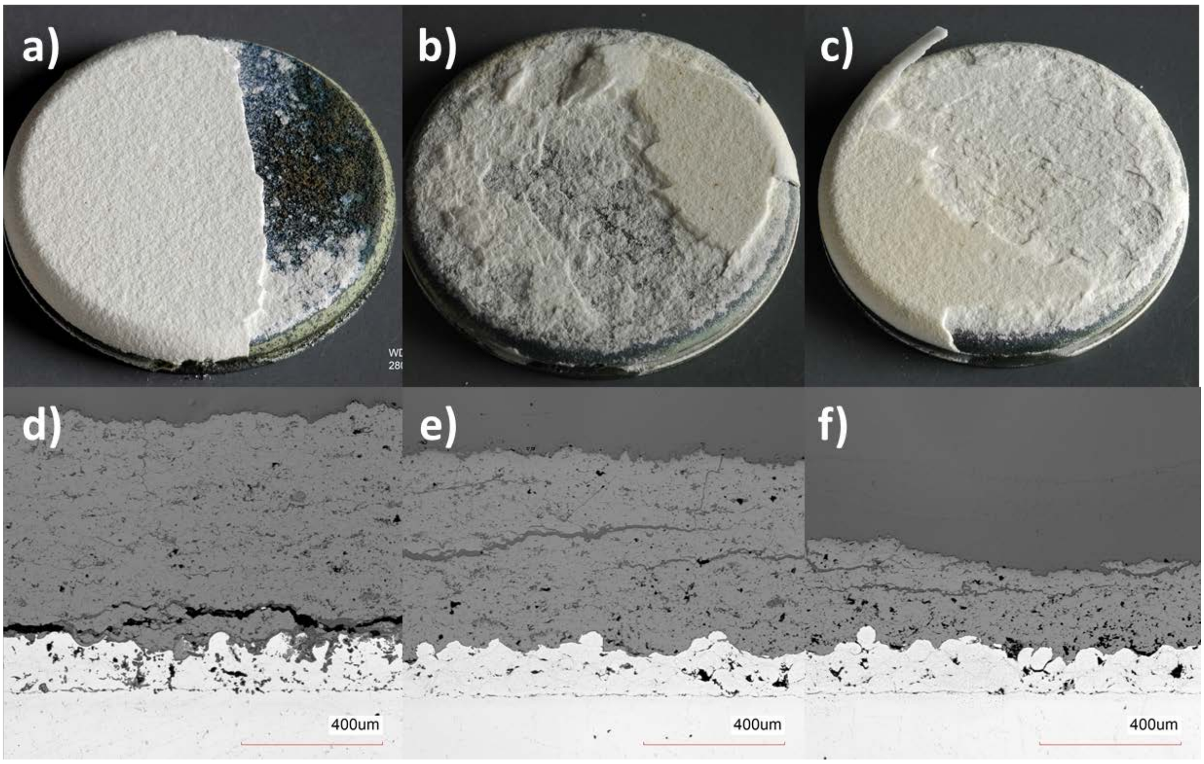

Figure 8: (prior Figure 7)

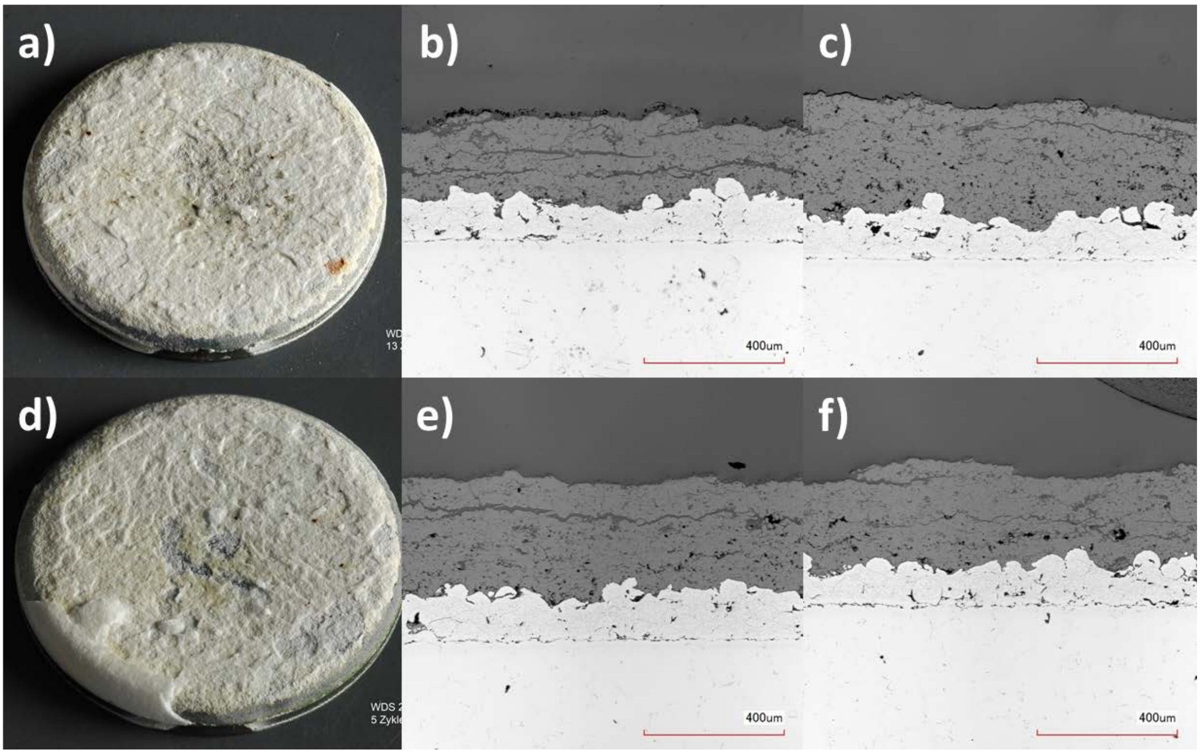

Figure 9: (prior Figure 8)

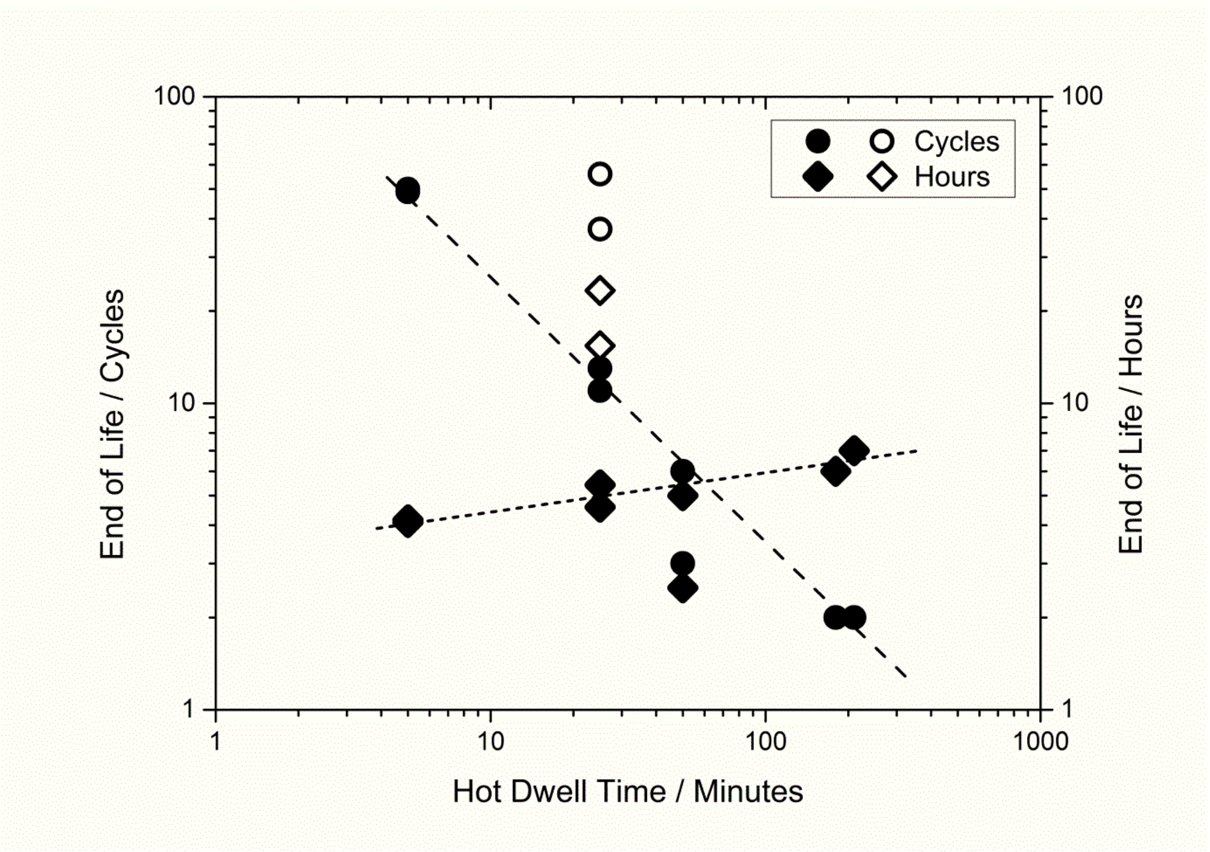

Figure 10: (prior Figure 9)

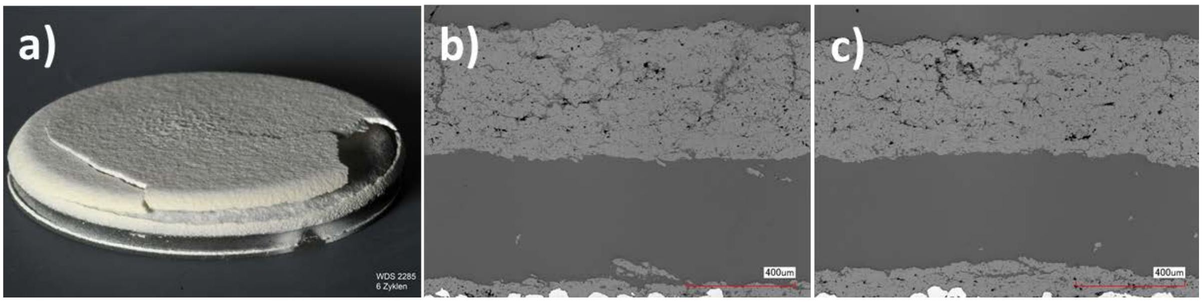

Figure 11: (prior Figure 10)

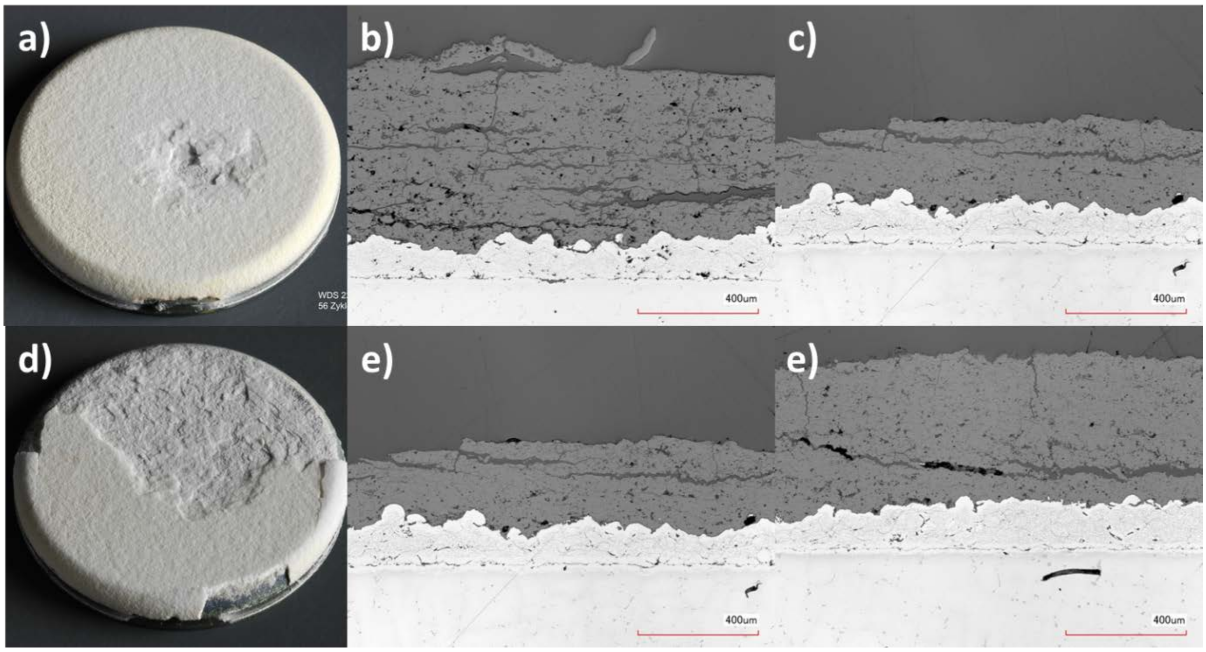

Figure 12: (prior Figure 11)